Available online at www.sciencedirect.com
ScienceDirect
Polymer 49 (2008) 757–773
polymer
www.elsevier.com/locate/polymer

Gas permeability, solubility and diffusivity in 1,2-polybutadiene containing brookite nanoparticles

Scott Matteucci [a], Victor A. Kusuma [a], Steve Swinnea [b], Benny D. Freeman [a,*]

[a] Department of Chemical Engineering, The University of Texas at Austin, 10100 Burnet Road, Building 133, Austin, TX 78758, United States
[b] Texas Materials Institute, College of Engineering, The University of Texas at Austin, 1 University Station C2201, Austin, TX 78712, United States

Received 20 October 2007; accepted 9 December 2007
Available online 14 January 2008

Abstract

Brookite (*i.e.*, titanium dioxide) nanoparticles having a nominal diameter of 3 nm were dispersed in 1,2-polybutadiene (PB) via solution processing to form polymer nanocomposites. Atomic force microscopy and scanning transmission electron microscopy were used to characterize particle dispersion. A significant population of nanoparticle aggregates exhibited characteristic dimensions below 50 nm. However, some aggregates were over 1 μm in size. At high nanoparticle loadings (*e.g.*, 27 nominal volume percent TiO_2), the permeability coefficients of CO_2, CH_4, N_2 and H_2 were more than 3 times higher than that in unfilled PB, which is opposite to the trend typically observed when impermeable particles are added to rubbery polymers. Gas solubility coefficients generally increased with increasing particle loading, whereas diffusion coefficients decreased with increasing particle loading. Therefore, the increase in permeability was due to an increase in gas solubility upon incorporating highly sorbing nanoparticles into the polymer. Interestingly, there was virtually no change in pure gas selectivity in the nanocomposites as compared to unfilled PB.

Keywords: Nanocomposite; Poly(butadiene); Brookite

1. Introduction

Traditionally, doping rubbery polymers with non-porous, impermeable particles decreases gas permeability [1]. For example, Barrer et al. dispersed micron-sized ZnO particles in natural rubber; and permeability decreased with increasing particle loading which was in good agreement with predictions from composites theory [1]. Recently, a wide variety of very small particles have become available, and there has been rather general interest in understanding how such particles influence transport properties. In this regard, many groups have incorporated nanoparticles with high aspect ratios (*e.g.*, rods or flakes) into various polymeric membranes to reduce gas permeability [2–4]. For example, the O_2 permeability of polyesteramide containing 13 wt% octadecylammonium-treated montmorillonite clay, where the clay platelets were oriented parallel to the film surface, was 80% lower than that of the unfilled polymer, so the presence of even rather low concentrations of nanoparticles can profoundly reduce permeability [4].

The use of nanoparticles to alter permeation properties extends beyond reducing permeability with increasing filler content. For example, nanocomposites have been prepared whose permeability increases as particle loading increases [5–8]. Gas permeability in certain filled high free volume, glassy, substituted acetylene polymers increases by as much as fourfold as particle loading increases, and there is no significant change in pure gas selectivity values [8]. In other disubstituted polyacetylene nanocomposites, light gas permeability is as much as 30 times higher than that of the unfilled polymer. However, in these materials, selectivity decreased with increasing particle loading [9]. In another case, poly(4-methyl-2-pentyne) (PMP) exhibited an increase in both mixed gas permeability and selectivity as the concentration of fumed silica increased. Specifically, *n*-butane/CH_4 selectivity increased

* Corresponding author. Tel.: +1 512 232 2803; fax: +1 512 232 2807.
E-mail address: freeman@che.utexas.edu (B.D. Freeman).

0032-3861/$ - see front matter © 2007 Elsevier Ltd. All rights reserved.
doi:10.1016/j.polymer.2007.12.011

from 13 in unfilled PMP to 22 in PMP containing 45 wt% fumed silica [10]. Additionally, the permeabilities of some low free volume, glassy polymers increase with increasing particle loading [11]. For instance, the reported O_2 permeability in solution cast Ultem 1000 filled with 20 wt% surface treated fumed silica was approximately 15 times higher than that of the unfilled polymer [11].

So far, only nanocomposites based on stiff chain, glassy polymers have been reported to exhibit light gas permeabilities higher than those of the comparable unfilled polymer. Rubbery polymers have not been shown to exhibit permeability enhancements with increasing nanoparticle concentration [12]. This study presents the influence of 3 nm diameter titanium dioxide (TiO_2) nanoparticles on gas transport properties of 1,2-polybutadiene (PB)-based nanocomposites. We find that the dispersion of nanoscale TiO_2 particles into PB can substantially increase its permeability without introducing selectivity-destroying defects. Pure gas permeability, solubility and diffusion coefficients are reported as a function of nanocomposite particle concentration. Atomic force microscopy and scanning transmission electron microscopy were used to characterize particle dispersion. Changes in polymer glass transition temperature and crystallinity with particle content were characterized using differential scanning calorimetry and wide angle X-ray diffraction, respectively.

2. Background

2.1. Gas transport in polymers

Gas transport through dense polymer films obeys the solution-diffusion mechanism, where gases dissolve into the polymer matrix at the face of the sample exposed to higher gas pressure, diffuse across the polymer film to the face of the sample exposed to lower pressure, and then desorb from that surface [13]. The permeability of gas A, P_A, through a film is defined as follows [13]:

$$P_A \equiv \frac{N_A l}{(p_2 - p_1)} \tag{1}$$

where N_A is the steady state gas flux through the film, l is the film thickness, and p_2 and p_1 are the upstream (*i.e.*, high) and downstream (*i.e.*, low) partial pressures of gas A, respectively. If Fick's law is obeyed and the downstream pressure is much lower than the upstream pressure, then permeability can be expressed as follows [13]:

$$P_A = D_A \times S_A \tag{2}$$

where D_A is the effective, concentration-averaged diffusion coefficient of gas A in the film. The solubility coefficient of gas A in the polymer, S_A, is given by [13]:

$$S_A = C/p_2 \tag{3}$$

where C is the gas concentration in the polymer at the film surface in contact with gas at pressure p_2 [13].

The ability of a polymer to separate gases A and B is characterized by the ideal selectivity, $\alpha_{A/B}$, which is defined as the ratio of permeabilities [13]:

$$\alpha_{A/B} \equiv \frac{P_A}{P_B} \tag{4}$$

Substituting Eq. (2) into Eq. (4) provides a relationship between the ideal selectivity, the diffusivity selectivity, D_A/D_B, and the solubility selectivity, S_A/S_B:

$$\alpha_{A/B} = \frac{D_A}{D_B} \times \frac{S_A}{S_B} \tag{5}$$

Diffusivity selectivity depends primarily on the relative penetrant sizes and the size-sieving ability of the polymer [14]. Solubility selectivity is controlled primarily by the relative condensability of the penetrants and the relative affinity of the penetrants for the polymer matrix [14]. Both solubility and diffusivity can be influenced by particle type and concentration [1,8,10].

2.2. Modeling gas transport properties in heterogeneous films

Many models have been derived to describe electrical conductivity in materials composed of a dispersed phase in a continuous matrix, and these models have also been used to describe permeability in heterogeneous materials [1,15,16]. For example, Bruggeman's model has been used to describe permeability in heterogeneous materials over a wide range of particle loading [1,15,17,18]:

$$\frac{(P_C/P_M) - (P_D/P_M)}{1 - (P_D/P_M)} \left(\frac{P_C}{P_M}\right)^{1/3} = 1 - \phi_D \tag{6}$$

where P_C, P_M, and P_D are the permeabilities of the composite, polymer matrix, and dispersed phase, respectively. ϕ_D is the dispersed phase volume fraction. In this model, the dispersed phase comprises spherical particles. In heterogeneous films containing an impermeable dispersed phase (*i.e.*, $P_D = 0$), Eq. (6) reduces to [17]:

$$\frac{P_C}{P_M} = (1 - \phi_D)^{3/2} \tag{7}$$

If the dispersed phase is much more permeable than the matrix (*i.e.*, $P_D > P_M$), Eq. (6) becomes [17]:

$$\frac{P_C}{P_M} = \frac{1}{(1 - \phi_D)^3} \tag{8}$$

These limits are presented together with exemplary experimental data in Fig. 1 [1,9]. In Fig. 1, the CH_4 permeability of natural rubber filled with impermeable, micron-sized ZnO particles obeys Eq. (7) to a good approximation [1]. Eq. (8) provides a reasonable estimate of the CH_4 permeability in MgO filled poly(1-trimethylsilyl-1-propyne) (PTMSP), when

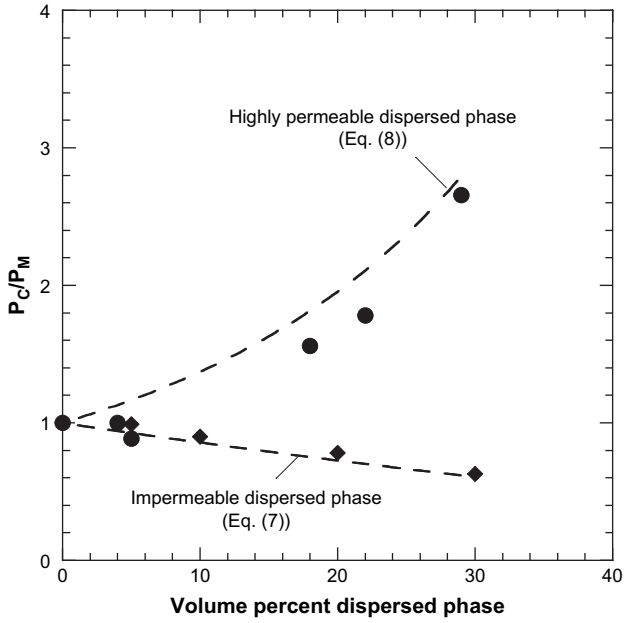

Fig. 1. Bruggeman's model for the ratio of composite permeability, P_C, to matrix permeability, P_M, when the dispersed phase is either impermeable (Eq. (7)) or highly permeable (Eq. (8)). Micron-sized ZnO filled natural rubber [1] at 40 °C and (◆) represents heterogeneous materials where the dispersed phase (ZnO) is essentially impermeable. MgO filled poly(1-trimethylsilyl-1-propyne) (PTMSP) at 35 °C and $\Delta p = 3.4$ atm [9] (●) represents a case where the nanoparticles induce void formation in the polymer, and these voids are presumably much more permeable than the polymer matrix. The voids are treated as the dispersed phase in the application of Eq. (8) to the PTMSP/MgO data.

the void volume, induced by incorporation of the particles in the polymer, is treated as the dispersed phase [9].

3. Materials and methods

3.1. Materials

Spherical brookite (*i.e.*, TiO_2) nanoparticles (Nanoscale, Manhattan, KS) were used in this study. The supplier reported the nanoparticles to be 99.999% titanium, based on metal, with a density of 3.7 g/cm^3 and a BET surface area of 500 m^2/g. The equivalent spherical particle diameter of the TiO_2 nanoparticles is 3 nm, where equivalent spherical particle diameter is calculated as 6/(surface area × density). 1,2-Polybutadiene (Scientific Polymer Products, Inc. Ontario, NY) has a molecular weight of approximately 100,000 and was prepared using a cobalt–phosphine catalyst system. According to the supplier, the 1,4-*cis* content was 7%, and the vinyl content was 93%. CH_4, CO_2, N_2, and H_2 were obtained commercially (Airgas, Radnor, PA). All gases used in this study were at least 99% pure according to the supplier. All materials and test gases were used as-received.

3.2. 1,2-Polybutadiene nanocomposite film preparation

1,2-Polybutadiene was added to toluene (1.5 g polymer/20 ml solution) and stirred at 40 °C until the polymer dissolved, which usually took less than 20 min. Nanoparticles were added to the solution in an amount that would result in a final dry film with a predetermined nominal filler volume percent loading, ϕ_F^N, which is defined as follows [8]:

$$\phi_F^N = \frac{M_F/\rho_F}{(M_P/\rho_P + M_F/\rho_F)} \tag{9}$$

where M_F and M_P are the weights of filler and polymer in the sample, respectively. ρ_F and ρ_P are the pure filler and pure polymer densities, respectively. The particle-filled solution was mixed for 20 min at 40 °C using a magnetic stir bar. The solution was poured onto a clean, dry, level glass casting plate in a fume hood and dried slowly. Films were generally dry in less than 24 h and resulted in nanocomposite films of around 200 μm thickness. The film thickness varied by less than 20 μm over the entire film surface. Permeability was not observed to depend on polymer thickness, where film thickness was varied from 100 to 400 μm.

3.3. Differential scanning calorimetry (DSC)

Polymer and nanocomposite samples weighing 10–20 mg were placed in steel DSC pans from TA Instruments (New Castle, Delaware). DSC sweeps were conducted using a Q-100 DSC from TA Instruments. The sweep began by lowering the sample temperature from ambient to −80 °C at 20 °C/min. The sample was held at −80 °C for 5 min and then heated at 20 °C/min to 150 °C. The maximum and minimum temperatures used in these sweeps were at least 40 °C away from the polymer melting temperature [19], and the range was sufficient to observe a complete melting event. Only the initial heating sweep is reported in this study, because subsequent sweeps alter the thermal history of the samples. DSC sweeps were conducted using an empty steel DSC pan as a reference.

The weight fraction of crystallinity in the unfilled polymer, χ_C (g crystals/g polymer), was calculated by comparing the polymer enthalpy of melting, ΔH_m, in the initial temperature sweep to the estimated enthalpy of melting of the pure crystalline polymer, ΔH_C:

$$\chi_C = \frac{\Delta H_m}{\Delta H_C} \tag{10}$$

ΔH_C for 1,2-polybutadiene is 60.7 J/g crystals [19]. This method was used to estimate the crystallinity in the unfilled polymer only. The neat particles showed an endothermic event at temperatures greater than 100 °C. As a result, in the nanocomposite films, there was an endothermic event between 120 and 150 °C that prevented reliable measurements of ΔH_m, so it was not possible to estimate the crystallinity level in the nanocomposites from DSC data.

3.4. Wide angle X-ray diffraction (WAXD)

A Scintag theta–theta diffractometer equipped with a Cu source and a solid state detector was used to collect wide angle X-ray diffraction (WAXD) patterns from approximately 3 cm^2

samples of 1,2-polybutadiene and nanocomposite films. To determine polymer crystallinity, backgrounds were modeled and removed from each diffraction pattern in a manner consistent with the literature [20]. An amorphous halo centered at about 14.5° 2θ was modeled for height, location, full width at half maximum (FWHM), and skew. Additionally, crystalline diffraction peaks for 1,2-polybutadiene were modeled for height, location and FWHM. χ_C was calculated from the WAXD data as follows [21]:

$$\chi_C = \frac{I_C}{I_C + I_A} \tag{11}$$

where I_C and I_A are the integrated areas under the crystalline and amorphous peaks, respectively.

3.5. Density

Sample density values were determined using a hydrostatic weighing method that employed a Mettler Toledo balance (Model AG204, Columbus, OH) and a density determination kit [22]. Deionized water with a resistance of 18.2 MΩ cm was used. The water was prepared using a Milli-Q plus TOC (Millipore, Billerica, MA).

The volume fraction crystallinity of the pure polymer, ϕ_C, was estimated from the experimentally determined polymer density, ρ_P, as follows [22]:

$$\phi_C = \frac{\rho_P - \rho_A}{\rho_C - \rho_A} \tag{12}$$

where ρ_C and ρ_A are the densities of crystalline (*i.e.*, 0.963 g/cm^3) [23] and amorphous (*i.e.*, 0.889 g/cm^3) [19] 1,2-polybutadiene, respectively. For the sample considered in this study, ρ_P was 0.911 ± 0.05 g/cm^3. The volume fraction crystallinity was converted to weight fraction as follows [21]:

$$\chi_C = \phi_C \frac{\rho_C}{\rho_P} \tag{13}$$

Density could not be used to determine the crystallinity of the polymer phase in the nanocomposite due to non-additive density behavior observed in the nanocomposites, as will be discussed below.

3.6. Atomic force microscopy (AFM)

The PB and nanocomposite samples were cut to a convenient size for microtoming, approximately 2 mm wide, using a razor blade. Tapering cuts were made to form a point on the sample, which was then polished to yield a small protruding rectangular surface. All samples were polished at −100 °C (*i.e.*, significantly below the glass transition temperature of 1,2-polybutadiene, which is reported to be −19 to −10 °C, depending on the crystallinity level and sample thermal history) [19] using an RMC-Boeckeler PowerTome PT-XL cryomicrotome (Boeckeler Instruments Inc., Tucson, AZ). For polishing, a cryo diamond knife (Micro Star Technologies, Huntsville, TX) was used at a cutting speed of 0.6 mm/s. To ensure sample stability for AFM surface analysis, the polished samples were mounted on AFM sample holders (Ted Pella Inc., Redding, CA) using 5-min epoxy (Fisher Scientific International Inc., Hampton, NH) with the polished side up.

Tapping mode AFM was used to characterize particle dispersion and aggregate size in film cross-sections. The AFM was a Digital Instruments Dimension 3100 with a Nanoscope IV controller (Woodbury, New York). AFM tips were Silicon NCH from Nanoworld (Neuchatel, Switzerland). Phase profiles were obtained over an area of 1 μm by 1 μm; 512 lines were scanned (scan rate 0.8 Hz) per sample, providing a resolution of 2 nm per line. All subsequent image analysis utilized ImageJ software from the National Institutes of Health, using a protocol discussed elsewhere [8].

Aggregate area distributions were obtained from AFM images using the ImageJ software. The distributions were divided into 100 bins of equal area increments, where the area increment of each bin was 4 nm^2. The use of a minimum of 50 bins ensured that the reported particle size and distribution were independent of the number of bins. The effective aggregate diameter for nanoparticles in bin j, d_j, was calculated using a spherical model:

$$d_j = \sqrt{\frac{4A_j}{\pi}} \tag{14}$$

where A_j is the apparent area of nanoparticle aggregates in bin j.

From the aggregate diameters and numbers of aggregates, an average diameter, $\overline{d}$, was calculated as follows [24]:

$$\overline{d} = \frac{1}{N_T}\sum_{j=1}^{m} d_j N_j \tag{15}$$

where N_j is the number of nanoparticle aggregates of diameter d_j. N_T is the total number of distinguishable aggregates characterized, which was generally around 500 aggregates per image. m is the total number of bins, which was set to 100 in this study. The standard deviation in aggregate size, σ, was calculated as follows [24]:

$$\sigma = \left(\frac{1}{N_T}\sum_{j=1}^{m}\left[\left(d_j - \overline{d}\right)^2 N_j\right]\right)^{1/2} \tag{16}$$

3.7. Scanning transmission electron microscopy (STEM)

Samples were trimmed using a razor blade in a manner similar to that described for the AFM samples. The trimmed samples were embedded in LR White resin (Electron Microscopy Sciences, Hatfield, PA) by cold curing in a BEEM® capsule container (Ted Pella Inc., Redding, CA). The embedded sample was pre-trimmed using a glass knife at room temperature with a Leica Ultracut UCT microtome (Leica Microsystems GmbH, Wetzlar, Hesse, Germany) to form a small, protruding, truncated pyramidal shape containing the sample with a smooth rectangular face approximately 100–200 μm

in length and width. Sections were collected from this pyramid using a cryo diamond knife operating at −100 °C at a cutting speed of 0.6 mm/s. The sections were floated on water in the diamond knife boat and deposited onto 400-mesh copper TEM grids (Ted Pella Inc.). High-angle annular dark field STEM images were collected using an FEI TECNAI G^2 F20 transmission electron microscope (FEI Company, Hillsboro, OR) operated at room temperature and an accelerating voltage of 200 kV.

3.8. Sorption

Gas sorption isotherms in polymer and nanocomposite samples were determined using a high-pressure barometric sorption apparatus as described elsewhere [25,26]. Prior to begin sorption experiments, vacuum was applied to the apparatus for at least 18 h to degas the film under study. Then, the degassed film was exposed to pure N_2, CH_4, and CO_2, in that order, at intervals of between 3 and 5 atm from vacuum to around 20 atm at 35 °C to measure a sorption isotherm over this pressure range.

3.9. Permeability

Pure gas permeability was determined using a constant volume/variable pressure apparatus [26,27]. A 13.8 cm^2 circular unmasked film was secured in the permeation cell. The film was exposed to vacuum for at least 18 h on both the upstream and the downstream surfaces to degas the sample. After a successful leak test, the downstream volume was evacuated (*i.e.*, downstream pressure was below 0.01 cmHg), and the upstream film surface was exposed to pure gas at a known pressure. Gas permeability (cm^3(STP) cm/(cm^2 s cmHg)) was calculated from the steady state rate of pressure increase in the downstream volume as follows:

$$P = \frac{dp}{dt}\frac{I \cdot V}{T \cdot p \cdot A \cdot R} \tag{17}$$

where dp/dt is the pseudo-steady state rate of pressure increase in the downstream volume, l is the film thickness (cm), p is the upstream absolute pressure, A is the area of the film available for transport (cm^2), V is the downstream volume (cm^3), and T is the absolute temperature (K). R is the gas constant. All experiments were performed with downstream pressure values below 1 cmHg.

4. Results and discussion

4.1. Nanocomposite stability

Nanoparticles have the potential to react either with the polymer matrix (*e.g.*, desilylation of poly[1-phenyl-2-[*p*-(trimethylsilyl)phenyl]acetylene] by MgO nanoparticles) [5] or with penetrant gases (*e.g.*, reaction of MgO with water) [28]. Therefore, care was taken to insure that such effects were not operative in this study. In this regard, TiO_2 is stable in the presence of water and the gases used in this study [8]. No chemical reaction was observed between TiO_2 and PB, based upon Fourier transform infrared spectroscopy of PB and PB-based nanocomposites.

4.2. Crystallinity and glass transition temperature in 1,2-polybutadiene and 1,2-polybutadiene based nanocomposites

Fig. 2 presents the WAXD sweeps for PB and PB−TiO_2 nanocomposites. The peaks in the unfilled PB are located at 13.2°, 16.0°, 21.6°, 24.0°, 35.0°, and 39.1° (2θ), and these values are consistent with the peak locations reported by Obata et al. for PB containing 32 wt% crystals [19]. All peaks in the unfilled polymer were also present in the nanocomposites. The crystalline peak located at 13.2° (2θ) in the unfilled polymer shifts to higher 2θ values in the nanocomposites as particle loading increases. Such a drift in this peak has been reported for unfilled PB samples as crystal content decreases [19]. As will be discussed below, the crystalline fraction of the polymer decreases as particle content increases. Thus, the shift in the peak at 13.2° (2θ) to higher values at higher particle loadings is consistent with the reduction in crystallinity observed as particle loading increases. On this basis, it appears that the nanoparticles have not changed the crystal structure.

Nanoparticles dispersed in rubbery polymers have been reported to nucleate polymer crystallite growth, which increases the crystalline content of the polymer in nanocomposites [29], or interfere with polymer crystallization, resulting in lower polymer crystallinity levels in the nanocomposite than in the unfilled polymer [30]. Table 1 presents crystallinity values for PB and PB-based nanocomposites. Fig. 3 presents the

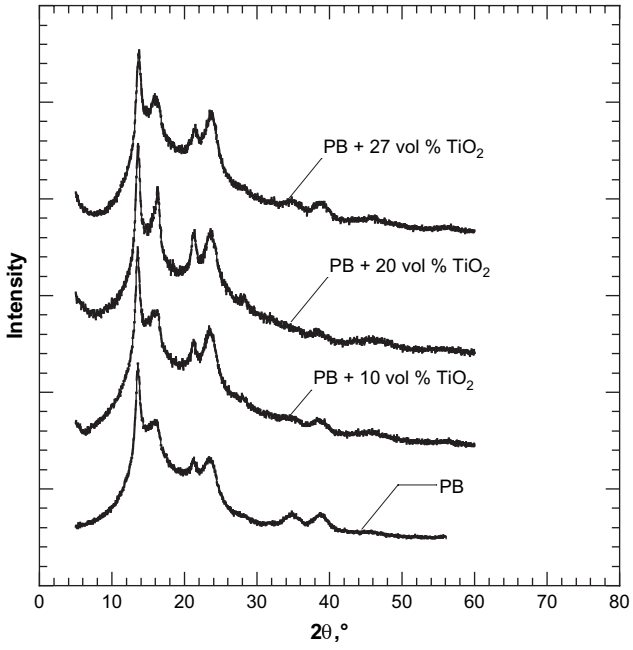

Fig. 2. WAXD patterns for TiO_2 nanoparticles, unfilled 1,2-polybutadiene, and 1,2-polybutadiene filled with 10, 20, and 27 nominal volume percent TiO_2. These spectra were displaced vertically for easier viewing.

Table 1
Polymer and nanocomposite crystallinity and glass transition temperatures

ϕ_F^N (%)	Technique for estimating crystallinity	χ_C (%)	ϕ_C (%)	T_g[b] (°C)
0	Density[a]	30 ± 5	28 ± 4	–
0	DSC	34 ± 3	32 ± 3	−17 ± 3
0	WAXD	32 ± 3	30 ± 3	–
10	WAXD	24 ± 1	22 ± 2	−9 ± 3
20	WAXD	23 ± 1	18 ± 2	−10 ± 3
27	WAXD	20 ± 1	15 ± 2	−9 ± 3

Note: uncertainties were estimated using the propagation of errors method [39].

[a] Density measurements yield a value of ϕ_C, which was converted to χ_C using Eq. (13). The other techniques considered (*i.e.*, DSC and WAXD) yield estimates of χ_C, which were converted to ϕ_C using Eq. (18).

[b] All glass transition temperatures were determined using first scan DSC data.

DSC scan from which the unfilled PB crystallinity was estimated. There are two discernable melting points for unfilled PB. The lower melting point, $T_{m,1}$, occurs at 60 °C, and the higher melting point, $T_{m,2}$, was 100 °C. Both melting point values agree with those reported by Obata et al. [19].

The estimates of crystallinity in the unfilled polymer from WAXD (*i.e.*, 32 ± 3 wt%) and density (*i.e.*, 30 ± 5 wt% as estimated by Eq. (13)) are quite similar, and these values are consistent with the value measured by DSC (*i.e.*, 34 ± 3 wt%). However, as shown in Table 1, the weight fraction of crystalline polymer in the polymer, χ_C, determined from WAXD and Eq. (11), is influenced by particle loading. χ_C decreases from about 32 wt% in the unfilled polymer to about 20 wt% in the samples containing 27 nominal volume percent nanoparticles. Such behavior is qualitatively consistent with the literature in which nanoparticles are reported to interfere with polymer crystallization [30].

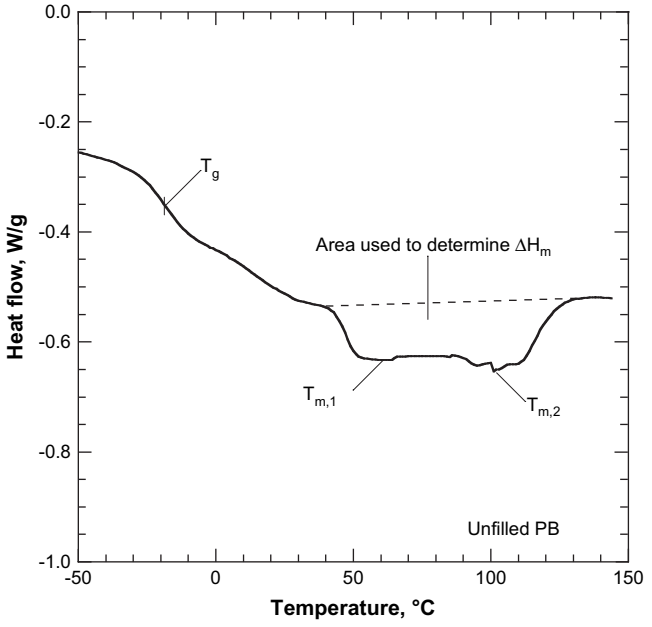

Fig. 3. DSC thermogram of unfilled PB. The data are from the first scan. The area between the dashed line and the thermogram (*i.e.*, the solid line) was used to determine ΔH_m. The glass transition temperature (T_g), the broad melting event, and the location of the melting temperatures ($T_{m,1}$ and $T_{m,2}$), are consistent with literature [19].

In some discussion to follow, it will be useful to have the crystallinity expressed in volume percent. Therefore, the volume fraction of crystalline PB in the polymer phase of the samples (*i.e.*, volume of crystalline polymer/total volume of polymer), ϕ_C was estimated as follows [21]:

$$\phi_C = \chi_C \frac{\rho_P^N}{\rho_C} \tag{18}$$

where ρ_P^N is the density of the polymer in the nanocomposite (*i.e.*, g polymer/cm^3 polymer), which was estimated as follows [19]:

$$\frac{1}{\rho_P^N} = \frac{\chi_C}{\rho_C} + \frac{\chi_C - 1}{\rho_A} \tag{19}$$

Eq. (19) assumes that the amorphous and crystalline phase polymer densities in the nanocomposite are not influenced by the presence of the nanoparticles. The volume fraction crystallinity values are recorded in Table 1.

In some polymer nanocomposites, the polymer glass transition temperature, T_g, is influenced by the concentration of nanoparticles [31,32]. For example, the bulk T_g of poly(2-vinyl pyridine) increased with alumina nanoparticle content from 100 °C in the unfilled polymer to 117 °C in a film containing 4 vol% alumina nanospheres [32]. Such increases in T_g have been ascribed to strong interactions between the polymer and the nanoparticles [32]. Table 1 presents T_g values in PB and the PB-based nanocomposites considered in this study. The thermograms from which the glass transition values are obtained are presented in Fig. 4. The T_g of the unfilled polymer is approximately 8 °C lower than that of the nanocomposite samples. This increase in T_g suggests reduced polymer chain mobility in the nanocomposite samples relative to the unfilled polymer. Such reductions in polymer chain mobility have been attributed to adsorption of polymer chains to nanoparticles, which effectively tethers the polymer to the particle [31,32].

The T_g of PB is known to decrease as crystallinity decreases [19]. For example, Obata et al. reported that the T_g decreases from 7 to −38 °C as crystallinity goes from 46 to 0 wt% [19]. On this basis, T_g should decrease, not increase, with increasing particle content if the only effect of the particles was to disrupt crystallinity. Therefore, the observed increase in T_g due to the presence of the particles is even more significant when viewed in the light of the observed decrease in crystallinity, which should decrease T_g, with increasing particle content. Also, data to be presented later suggest that other phenomena (*e.g.*, voids or larger particle aggregates) may not interact with the bulk polymer in the same manner as individually dispersed particles or nanoscale particle aggregates. Such effects might explain why there is little change in T_g as nanoparticle content increases from 10 to 27 nominal volume percent. Therefore, several competing factors could be influencing the glass transition behavior of the nanocomposites.

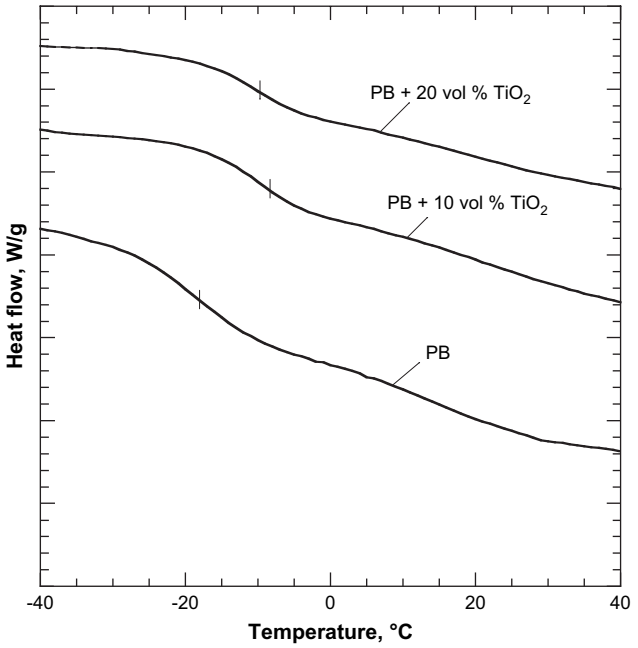

Fig. 4. Influence of nominal particle volume percent on the glass transition temperature of 1,2-polybutadiene filled with TiO_2 nanoparticles. The tick marks represent the T_g, which is identified as the midpoint of the endothermic step change in the heat capacity in the DSC thermograms. The data are from the first scan. The DSC traces have been displaced vertically for easier viewing.

4.3. Particle dispersion

Particle and aggregate dispersion influence gas transport in heterogeneous nanocomposite films [2,6,8,10,11,33]. AFM tapping mode phase profiles can be used to resolve the relative modulus of polymer and nanocomposite samples [34]. This technique can resolve individual nanoparticles that are in the order of several nanometers in primary particle diameter since the nanoparticle modulus is expected to be much greater than that of the polymer. That is, the nanoparticles typically constitute the hard phase, and the polymer is the soft phase in nanocomposite samples. This situation is somewhat more complex in PB-based nanocomposites, since the polymer contains hard crystalline regions in addition to soft amorphous regions. This issue is discussed in more detail below.

Fig. 5 presents AFM phase profiles for unfilled PB and PB-based composites containing 7 and 20 nominal volume percent TiO_2. In Fig. 5a, the neat PB exhibits two distinct phases. The phase with the higher modulus appears lighter, while the softer, lower modulus phase is darker. The phase with the higher modulus in this image is attributed to crystalline PB, and the softer phase is ascribed to amorphous PB. The high modulus phase occupies approximately 27 area percent of Fig. 5a, which is consistent with the crystalline volume percent (28–32%) recorded in Table 1.

Fig. 5b and c presents images of PB nanocomposites. The dark lines in Fig. 5c are artifacts caused by contaminants (*i.e.*, nanoparticles) on the sample surface or AFM cantilever tip [35]. There are also two distinct phases in these images. The hard phase occupies ~7 and 23% of the area of Fig. 5b and c, respectively, which are essentially the same as the nominal volume percent nanoparticles in the sample (*i.e.*, 7 and 20 nominal volume percent, respectively), suggesting that the hard phase in the nanocomposites is particles or particle-rich regions.

The nanoparticle modulus may be sufficiently high, relative to that of the polymer matrix that it is not possible to distinguish between the crystalline and the amorphous polymer phases. Based on the literature, AFM phase profile images have produced mixed results when used to characterize nanoparticle-filled semi-crystalline polymers. In certain systems, the crystalline polymer phase cannot be resolved [36]. In other cases, the nanoparticles did not appear on the images [37]. Finally, some groups have resolved both crystalline polymer and nanoparticles in such systems [38].

According to the WAXD results in Table 1, the polymer crystallinity (*i.e.*, the volume of crystals per unit volume of polymer) decreases as particle loading increases, which is opposite to the trend observed in Fig. 5b and c, where the area fraction occupied by the hard phase increases with increasing particle concentration. Based on all of this information, the hard phase in Fig. 5b and c is ascribed to nanoparticles and not to polymer crystals.

Image analysis can be used to estimate the average diameter, $\overline{d}$, of the harder phase in the nanocomposite AFM images using Eq. (15). The nanoparticle aggregates in Fig. 5b have an estimated average diameter of 9 ± 4 nm. Distributions were not estimated for Fig. 5c, since there are relatively few aggregates in this image, and many of the aggregates do not fit within the image boundaries. The fraction of aggregates of diameter d_j, F_j, can be calculated as follows:

$$F_j = \frac{N_j}{N_T} \tag{20}$$

The nanoparticle aggregate diameter distribution is presented in Fig. 6 for PB containing 7 nominal volume percent TiO_2.

The distribution of aggregate diameters can be further characterized by fitting the data in Fig. 6 to a Weibull distribution, which is often used to characterize particle size distributions [24,39,40]:

$$F_j = \frac{\beta}{\alpha}\left(\frac{d_j - \upsilon}{\alpha}\right)^{\beta-1} \exp\left[-\left(\frac{d_j - \upsilon}{\alpha}\right)^{\beta}\right] \tag{21}$$

where υ is the nanoparticle diameter, and β and α are fitting parameters. In this calculation, d_j must be $\geq \upsilon$. $\overline{d}$ was 9 ± 6 nm as determined from the Weibull distribution, as follows [24]:

$$\overline{d} = \sum_{j=1}^{h} d_j F_j \tag{22}$$

where h is the number of bins used in the AFM particle analysis (*i.e.*, 100). Based on the particle distribution data in Fig. 6, a significant percentage of particles are dispersed

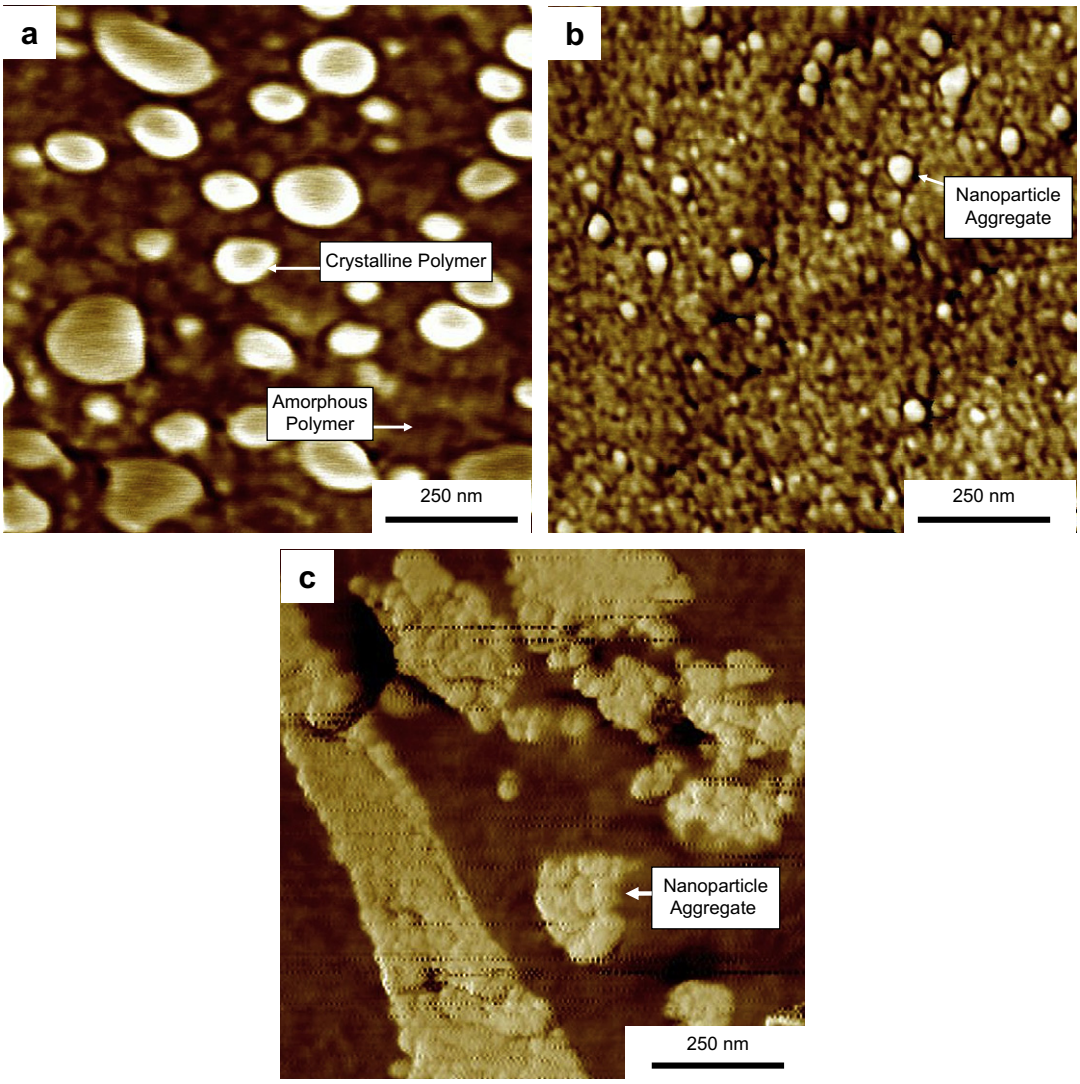

Fig. 5. 1 μm by 1 μm tapping mode AFM phase profiles of (a) PB, (b) PB containing 7 nominal volume percent, and (c) 20 nominal volume percent TiO_2. Dark regions correspond to soft (*i.e.*, low modulus) material and less dark (*i.e.*, white) regions correspond to hard material.

individually or in small nanoparticle aggregates in PB filled with 7 nominal volume percent TiO_2.

The average inter-aggregate distance, d_a, can be estimated by assuming that the aggregates are spherical and dispersed in a body centered cubic structure [8]:

$$d_a = \overline{d}\left[\left(\frac{\pi}{6\phi_F^N}\right)^{1/3} - 1\right] \tag{23}$$

where $\overline{d}$ is the average aggregate diameter (nm), and ϕ_F^N is the nanoparticle volume fraction in the composite as calculated from Eq. (9). The use of either ϕ_F^N (*i.e.*, the nominal volume fraction of filler) or ϕ_F^T (*i.e.*, the true volume fraction of filler, that is the volume of filler per unit volume of nanocomposite sample) in Eq. (23) does not change the results significantly. ϕ_F^N is used in Eq. (23) since it is used in other calculations in this study, as will be presented below. A discussion of the differences between ϕ_F^N and ϕ_F^T is presented later. A body centered cubic aggregate structure is assumed to simplify estimates of d_a. More realistic structures, such as a random aggregate distribution [41], yield very similar values for d_a. PB films containing 7 nominal volume percent TiO_2 exhibit d_a values of approximately 9 nm, which is similar to the inter-aggregate spacing for TiO_2 nanoparticles dispersed in a glassy polymer, PTMSP, where d_a was 9 and 11 nm for 3 and 10 nominal volume percent TiO_2, respectively [8]. The interparticle spacing in these nanocomposites is comparable to the size of structural features of PB molecules. For instance, the radius of gyration of 1,2-polybutadiene of a molecular weight of 100,000 is 8.5 nm [42]. On this basis, one might anticipate that having nanoparticles dispersed at spacings that are comparable to the polymer chain size could have a substantial influence on the properties of such systems.

Since the individual nanoparticles are approximately the same size as the resolution of the AFM images, any particles with characteristic diameters below the resolution limits would not be included in calculations of $\overline{d}$ or d_a. This effect may

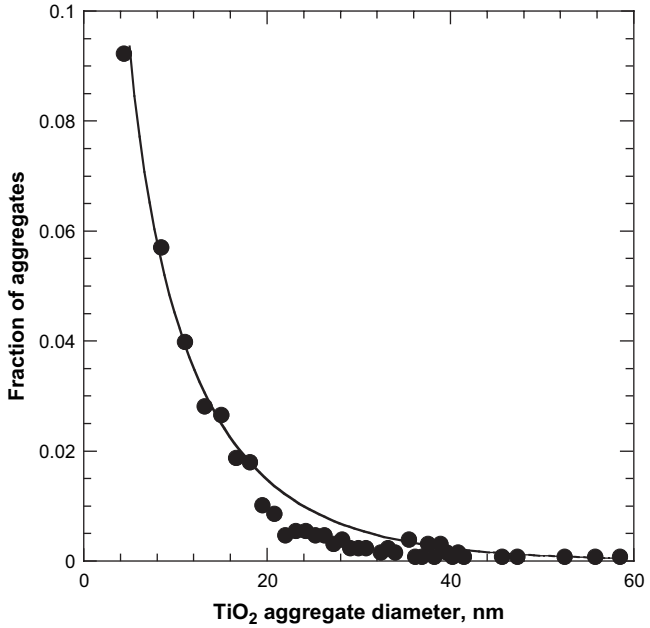

Fig. 6. TiO_2 aggregate diameter distribution from tapping mode phase profiles of PB containing 7 nominal volume percent TiO_2. The solid line represents a Weibull distribution using $v = 3.0$ nm, $\beta = 8.40 \pm 5.00$ and $\alpha = 0.86 \pm 0.59$ [24,40]. Uncertainties in the Weibull distribution parameters were determined by a least-squares fit method [39].

cause the reported average aggregate diameter and average inter-aggregate spacing value to be somewhat higher than the true values. Therefore, the $\overline{d}$ or d_a values reported in this paper are most likely higher than the actual values.

Many aggregates in Fig. 5c are on the order of microns in characteristic dimensions. At these loadings, individually dispersed nanoparticles and small aggregates (*i.e.*, aggregates with <100 nm characteristic diameter) cannot be resolved. It is possible at these loadings that TiO_2 nanoparticles cannot effectively disperse in the polymer, which may be related, in part, to the elevated solution viscosity and, therefore, to a lack of effective mixing, when large amounts of nanoparticles are added to the PB–toluene solution.

Dark field STEM can be used to resolve micron-sized aggregates. Examples of such aggregates are present in Fig. 7 for PB containing 7 and 13 nominal volume percent TiO_2. Since the nanoparticles are expected to have the highest electron density of the phases present in the nanocomposite, the large light structures in the STEM images are attributed to nanoparticle aggregates. The aggregates shown at these loadings are representative of aggregates observed in other TiO_2 filled PB nanocomposite samples. Since STEM distinguishes features in materials based on differences in electron density, the nanoparticle-rich (*i.e.*, electron-rich, as shown in white) and the polymer-rich (*i.e.*, electron-poor, as shown in black or dark gray) regions are readily observed. The presence of these aggregates may be due to poor particle mixing with the polymer, poor polymer–particle interaction, or the nanoparticle concentration reaching levels beyond which the nanoparticles cannot readily disperse individually or in small aggregates.

In summary, the dispersion of these nanoparticles in PB ranges from single particles dispersed in the polymer matrix to micron-sized aggregates of many particles. No single microscopic tool considered can capture the complete distribution of particles and particle aggregates in these samples. The use of multiple techniques, such as AFM and STEM, provides a better understanding of the particle dispersion. However, this is clearly an area where better analytical tools, capable of characterizing a very wide range of particle sizes, would be useful.

4.4. Nanocomposite density and void space

If the density of the nanoparticles, crystalline polymer and amorphous polymer phases has their pure component values in the nanocomposites, then the density of a nanocomposite

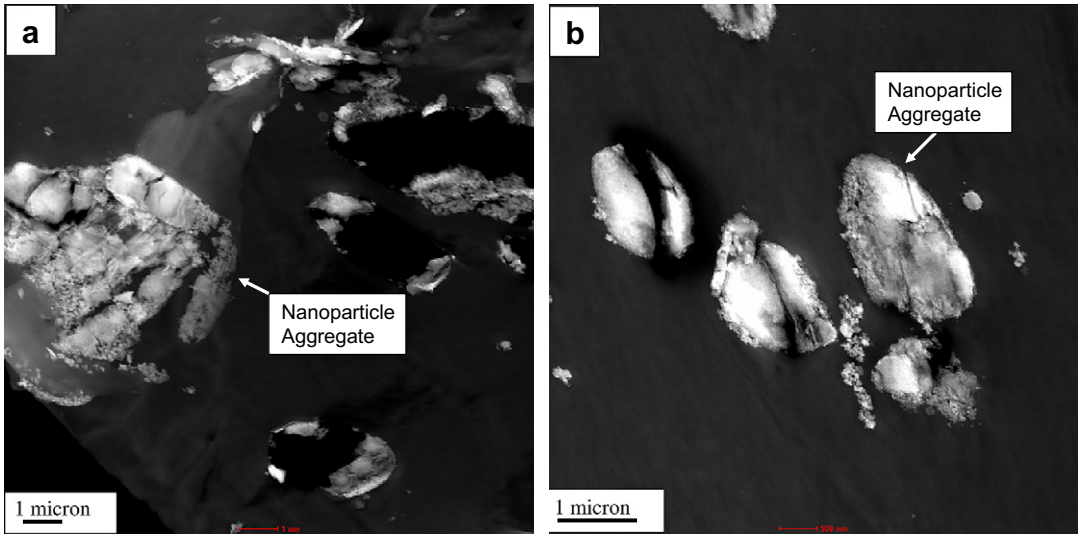

Fig. 7. STEM dark field image of (a) PB containing 7 nominal volume percent and (b) PB containing 13 nominal volume percent TiO_2. Electron-rich phases (*i.e.*, nanoparticles) are shown in white.

sample, ρ_{Exp}, would be equal to the theoretical additive density, ρ_{Add}, which is defined as follows:

$$\rho_{Add} = \phi_F^N \rho_F + \left(1 - \phi_F^N\right)\left(\phi_C \rho_C + (1 - \phi_C)\rho_A\right) \quad (24)$$

where ρ_F is the pure filler density. ϕ_C is the volume fraction of crystalline polymer (*i.e.*, volume of crystals per unit volume of polymer in the nanocomposites) (*cf.*, Table 1). That is, the additive density is the density of a semi-crystalline nanocomposite sample if each phase contributed to the nanocomposite density according to its pure component density value and the amount of each phase present.

Dispersing TiO_2 nanoparticles in PB increases the density of the nanocomposites, as shown in Fig. 8. However, ρ_{Exp} is less than ρ_{Add} at all TiO_2 loadings. The difference between ρ_{Exp} and ρ_{Add} can be rationalized by the creation of void space in the composite with increasing particle loading [8]. The void space can be expressed in terms of a void volume fraction, ϕ_V, defined as follows [8]:

$$\phi_V = \left(1 - \frac{\rho_{Exp}}{\rho_{Add}}\right) \quad (25)$$

Using Eq. (25), void volume fraction values were calculated and are presented as a function of nanoparticle concentration in Fig. 9. The void content increases with increasing particle loading, qualitatively consistent with previous results reported for glassy PTMSP filled with TiO_2 [8], and glassy polyether imide (*i.e.*, Ultem 1000) filled with surface treated fumed silica [11]. So far, microscopy has not been able to determine the location of such voids. We speculate that the voids may be located at the polymer–particle interface, in the interparticle spacing, or within nanoparticle aggregates [1,11,43].

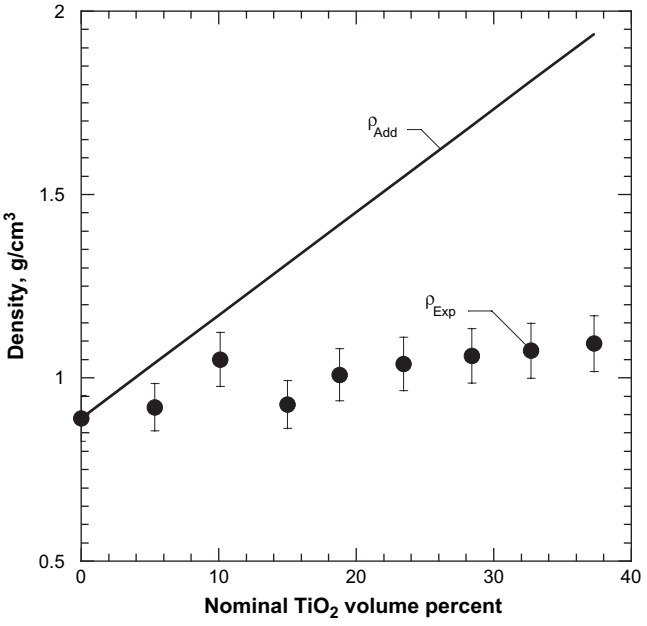

Fig. 8. Effect of TiO_2 concentration on nanocomposite density. ρ_{Exp} is the experimentally measured density and ρ_{Add} is the additive density predicted by Eq. (24). Error bars were estimated from the variance in density for multiple experiments at each point according to the propagation of errors method [39].

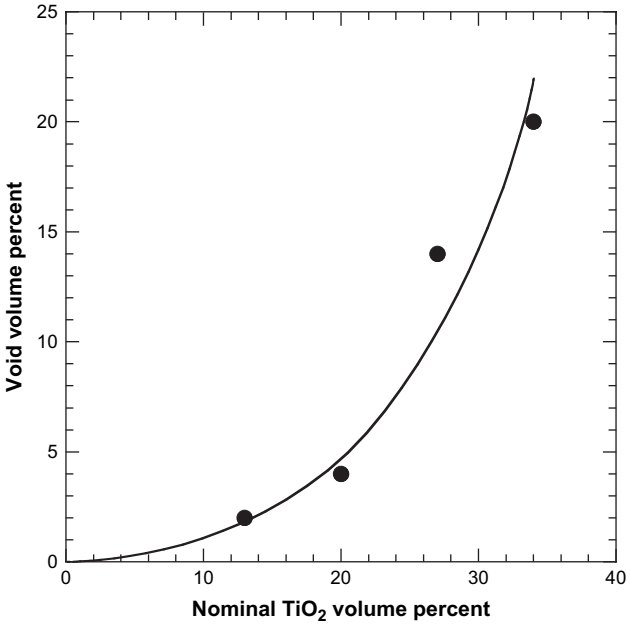

Fig. 9. Effect of particle concentration on nanocomposite void volume percent as estimated by Eq. (25). The trend line is drawn to guide the eye.

Based on these data, the true volume fraction of particle in the nanocomposite system, ϕ_F^T, may be calculated as follows [8]:

$$\phi_F^T = \phi_F^N (1 - \phi_V) \quad (26)$$

Using Eq. (26) and the data in Figs. 8 and 9, the maximum difference between ϕ_F^T and ϕ_F^N occurs at the maximum particle loadings, where ϕ_F^T is 18% and ϕ_F^N is 27%.

4.5. Gas transport in TiO_2 filled 1,2-polybutadiene

Fig. 10a presents the influence of particle loading on CO_2, CH_4, N_2, and H_2 permeability relative to the permeability of each gas in the unfilled polymer. As indicated in this figure, the permeability increases with increasing particle concentration. These data are compared to Bruggeman's model in the limit when the dispersed phase concentration is equal to the void volume (*i.e.*, Eq. (8) with $\phi_D = \phi_V$) in Fig. 10b. The permeability of all gases increases with increasing void volume, although the observed increase in permeability exceeds the increase anticipated by this model. Bruggeman's model does not account for any changes in the continuous phase permeability due to changes in solubility (*e.g.*, from adsorption of light gases on a nanoparticle surface) or changes in polymer phase crystallinity [17]. Bruggeman's model, as presented in Eq. (6), assumes that the dispersed phase is spherical [44]. If the dispersed phase is arranged in a non-spherical geometry, Eq. (6) is less accurate [15]. Deviations from these assumptions could cause the permeability of the filled polymer, based on expectations from the model calculations, to differ from the experimental data. Nonetheless, using Bruggeman's model in

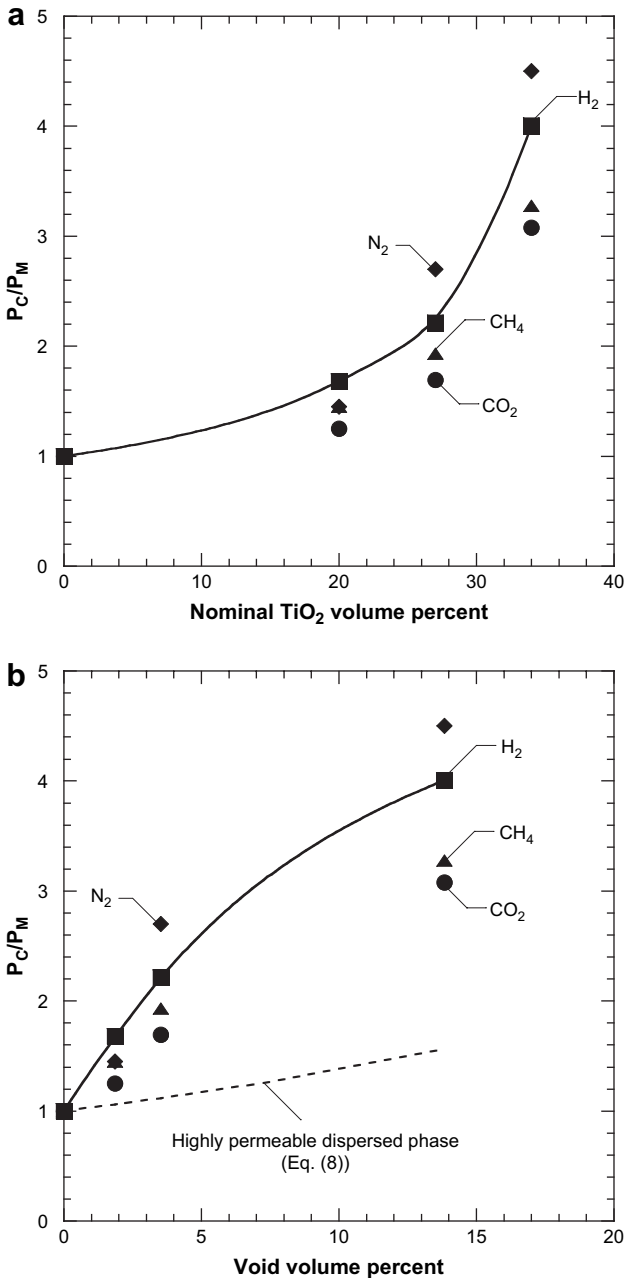

Fig. 10. Effect of dispersed phase concentration on the ratio of nanocomposite CO_2 (●), CH_4 (▲), N_2 (◆) and H_2 (■) permeability, P_C, to that of unfilled PB, P_M, where the dispersed phase is (a) nominal TiO_2 volume percent and (b) void volume percent calculated from Eq. (25). The dashed line represents Bruggeman's model (*i.e.*, Eq. (8)). The experimental data were measured at 35 °C and $\Delta p = 4.4$ atm. The solid line is drawn to guide the eye.

this fashion provides a rough estimate of the influence of the voids on the gas permeability in these nanocomposites. Within the scope of the approximations described above, a substantial portion of the increase in permeability must result from the effect of the TiO_2 nanoparticles on the gas transport properties of the solids (*i.e.*, polymer and particles) in the nanocomposite samples.

If the permeability enhancements were caused by *trans*-film defects, light gas permeability could increase with increasing upstream pressure depending on the size of the defects [45–47]. Also, selectivity values would trend towards values expected based on Knudsen or Poiseuille flow, depending on the size of the defects [45–47]. As will be demonstrated, neither of these effects is observed, suggesting that the increase in permeability does not derive from pinhole defects in the nanocomposite samples. For example, Fig. 11 presents gas permeability as a function of pressure for PB and a representative group of nanocomposites. The permeability values for unfilled PB are in good agreement with those reported by Naito et al., where CO_2, CH_4, N_2, and H_2 permeabilities were 43, 5.5, 1.9, and 30 barrer at 25 °C, respectively [48]. As Fig. 11 shows, CH_4, N_2, and H_2 permeabilities are independent of upstream pressure. Only CO_2 permeability increases with increasing pressure in the nanocomposite samples, which is attributed to plasticization of the polymer by CO_2 [13]. The permeability of CO_2 also increases slightly in unfilled PB with increasing pressure, which agrees with the literature [48]. However, the increase is masked by the overall scale of Fig. 11a. Loading particles into PB may intensify the increase in CO_2 permeability with increasing pressure, because the nanoparticles increase the concentration of CO_2 in the film, as discussed below, which may facilitate plasticization.

The Knudsen selectivity, $\alpha^K_{A/B}$, is given by [46]:

$$\alpha^K_{A/B}\sqrt{\frac{M_B}{M_A}} \tag{27}$$

where M_A and M_B are the molecular masses of penetrants A and B, respectively. The Poiseuille selectivity limit for gases tested individually, $\alpha^P_{A/B}$, is [47]:

$$\alpha^P_{A/B} = \frac{\mu_B}{\mu_A} \tag{28}$$

where μ_A and μ_B are the viscosities of gases A and B, respectively. Of course, the Poiseuille selectivity is 1 for mixtures of gases flowing through pores. Table 2 presents the selectivity limits for Knudsen and Poiseuille flow regimes for a number of gas pairs [9]. As shown in Fig. 12 for CO_2/light gas pairs, selectivity values in the nanocomposite samples do not vary perceptibly from those observed in the unfilled polymer. These selectivity values are not consistent with either Knudsen or Poiseuille selectivity. Since CH_4, N_2, and H_2 permeabilities are independent of upstream pressure, and the ideal selectivities are not at the Knudsen or Poiseuille flow limits, the permeability enhancements shown in Figs. 10 and 11 are not caused by transmembrane defects introduced by having the TiO_2 particles in the samples. Interestingly, as will be shown below, the permeability enhancement is due mainly to an increase in gas solubility as particle concentration increased.

At high nanoparticle loadings (*i.e.*, greater than 30 nominal volume percent), light gas selectivity values decreased to values suggesting the presence of transmembrane defects. Such non-selective nanocomposite materials have not been considered further in this study.

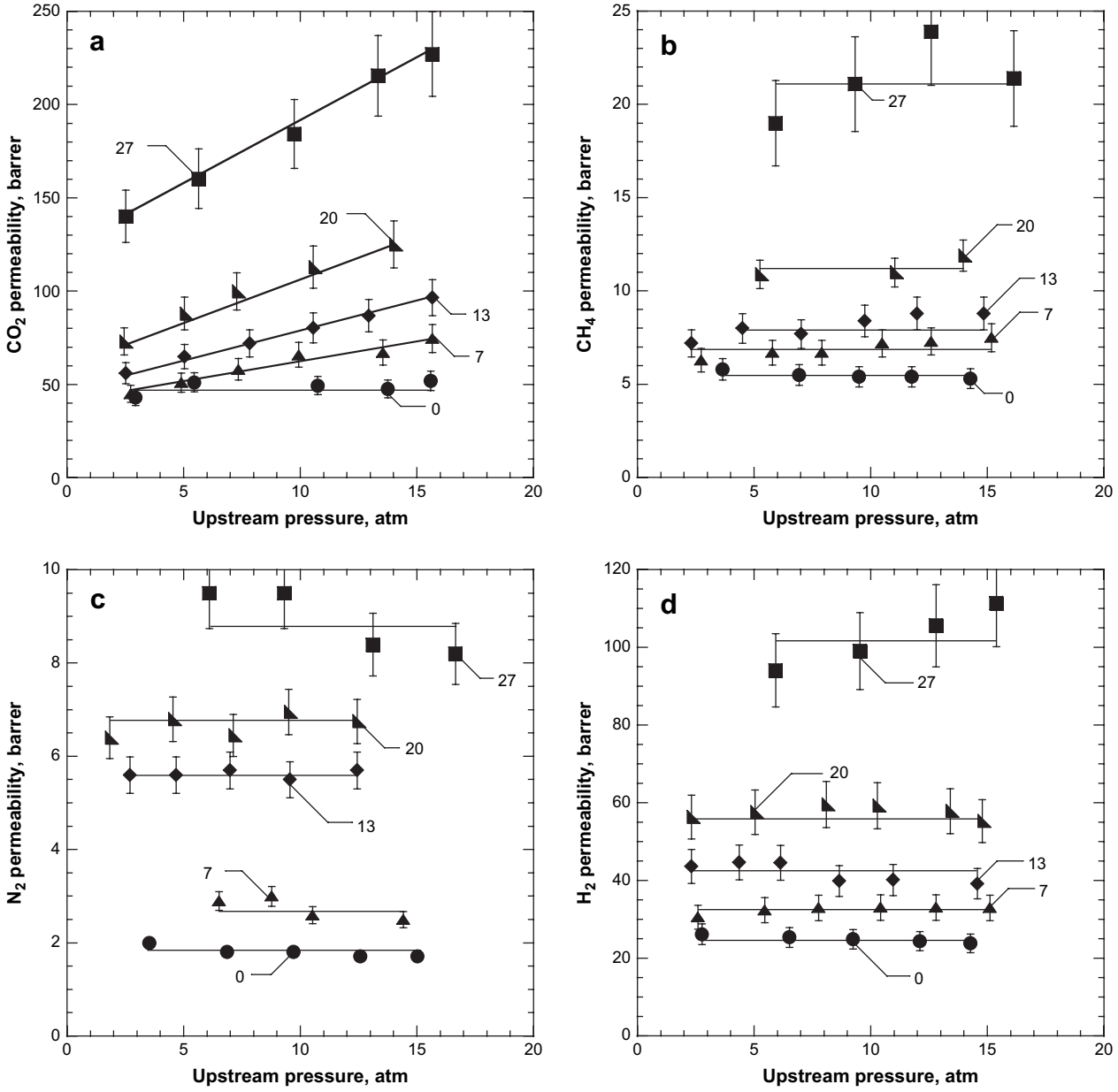

Fig. 11. Effect of upstream pressure on pure gas permeability in PB containing TiO_2 (a) CO_2, (b) CH_4, (c) N_2, and (d) H_2. The numbers next to the data indicate the nominal volume percent of TiO_2. Measurements were conducted at 35 °C and with downstream pressure less than 0.01 atm. Error bars were estimated from the variance in permeability for multiple experiments at each point according to the propagation of errors method [39]. Trend lines are drawn to guide the eye.

The permeability behavior can be further explored by examining the influence of nanoparticle content on gas solubility and diffusivity. TiO_2 nanoparticles adsorb significant amounts of light gases, as shown in Fig. 13 [8]. In fact, as will be demonstrated shortly, the particles sorb far more gas per unit volume than the polymer. Interestingly, the particles do not become saturated with absorbed gases (*i.e.*, CO_2, CH_4 and N_2) at least up to 1 atm [8].

The Freundlich isotherm has been used to characterize gas adsorption on TiO_2 nanoparticles, C_f [49]:

$$C_f = Kp^{1/n} \tag{29}$$

where K and n are temperature dependent fitting parameters [49], which are listed in Table 3. The Freundlich model is used in our studies because it does not limit sorption of gases to one monolayer on the particle surface, whereas other models (*e.g.*, the Langmuir model) have this limitation [49]. As demonstrated elsewhere for another polymer/particle combination [8],

Table 2
Knudsen diffusion and Poiseuille flow selectivities [9]

Flow regime	CO_2/N_2	CO_2/CH_4	CO_2/H_2
Knudsen diffusion	0.8	0.6	0.2
Poiseuille flow	1.2	0.7	0.6

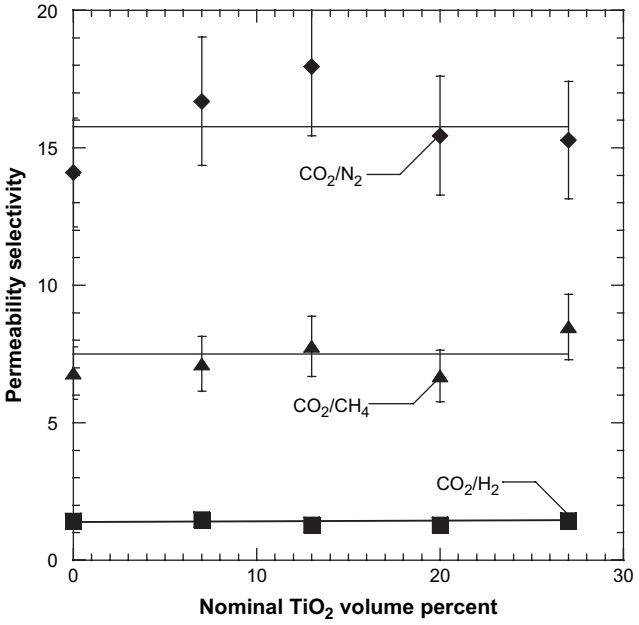

Fig. 12. Effect of particle concentration on pure gas CO_2/N_2 (◆), CO_2/CH_4 (▲), and CO_2/H_2 (■) permeability selectivity in PB nanocomposites. Experimental conditions were 35 °C and $\Delta p = 4.4$ atm. Trend lines are drawn to assist the reader. Error bars were estimated according to the propagation of errors method [39].

the Freundlich isotherm results in a better estimate of gas sorption in nanocomposites than the Langmuir model.

Light gas sorption in rubbery polymers, C_P, typically obeys Henry's law [13]:

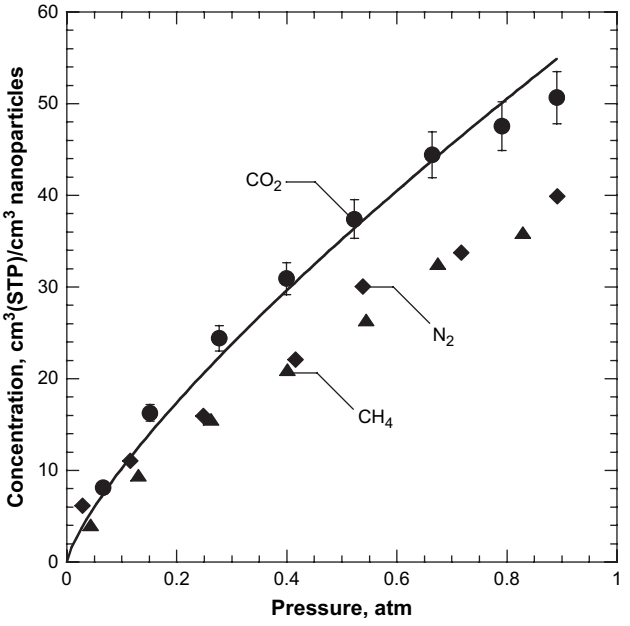

Fig. 13. Pure gas CO_2, CH_4, and N_2 adsorption isotherms on TiO_2 at 35 °C from the work of Matteucci et al. [8]. The solid line represents the Freundlich model (*i.e.*, Eq. (29)) for CO_2 adsorption on TiO_2 calculated using parameters from Table 3. Error bars were estimated from the variance in concentration for multiple experiments according to the propagation of errors method [39].

Table 3
Freundlich isotherm parameters for adsorption onto TiO_2 and Henry's law sorption parameters for 1,2-polybutadiene at 35 °C

Penetrant	K (cm^3(STP)/cm^3 TiO_2 $atm^{1/n}$)	n (-)	k_D (cm^3(STP)/cm^3 PB atm)	
			This work	Naito et al.
N_2	24 ± 7	1.8 ± 0.2	0.03 ± 0.01	0.04
CH_4	28 ± 8	1.4 ± 0.2	0.22 ± 0.02	0.23
CO_2	38 ± 10	1.4 ± 0.2	0.71 ± 0.06	0.81

Note: the Freundlich isotherm parameters are taken from the literature [8]. Henry's law constants were obtained from sorption experiments. Uncertainties were estimated using the least-squares fit method [39]. Naito et al. Henry's law parameters were determined at 25 °C [48].

$$C_P = k_D p \tag{30}$$

where k_D is Henry's law constant, and p is the gas pressure [13]. As Fig. 14 demonstrates, sorption isotherms in unfilled PB are linear, which is consistent with Henry's law and with the literature [48]. Henry's law parameters for CO_2, CH_4, and N_2 are recorded in Table 3. The k_D values obtained in this study are quite similar to those reported by Naito et al. [48].

k_D values should increase as crystallinity decreases. In general, crystalline polymers typically sorb a negligible amount of gas [50]. Therefore, a first estimate of Henry's law parameter in the amorphous region of a polymer is [51]:

$$k_{D,A} = \frac{k_D}{1 - \phi_{C,0}} \tag{31}$$

where $k_{D,A}$ is the estimated Henry's law parameter for amorphous polymer, and $\phi_{C,0}$ is the unfilled PB crystalline polymer volume fraction (cm^3 crystals/cm^3 polymer).

The concentration of gas in the void volume of a nanocomposite, C_V, can be estimated using the gas law [47]:

$$C_V = \left(\frac{p}{RT}\right) \tag{32}$$

The gas concentration in a nanocomposite, C_C, can be estimated using an additive model, where each phase is assumed to contribute its native gas sorption capacity to the overall gas concentration in the composite [8]:

$$C_C = \left(\phi_F^N K p^{1/n} + \left(1 - \phi_F^N\right)(1 - \phi_C) k_{D,A}\, p\right)(1 - \phi_V) + \frac{p\phi_V}{RT} \tag{33}$$

The first term in Eq. (33) represents the nanoparticle contribution. The second term is associated with the gas sorbed in the amorphous polymer phase, and the final term accounts for the concentration of gas in the voids.

According to Eq. (33), the contribution of the void volume and the amorphous polymer phase to the overall concentration of gas sorbed into the nanocomposite is linear with pressure. Generally, the contribution of the void volume to gas concentration is small relative to that of the polymer, due to the low concentration of voids in the nanocomposites. For instance, in a film containing 20 nominal volume percent TiO_2 (and

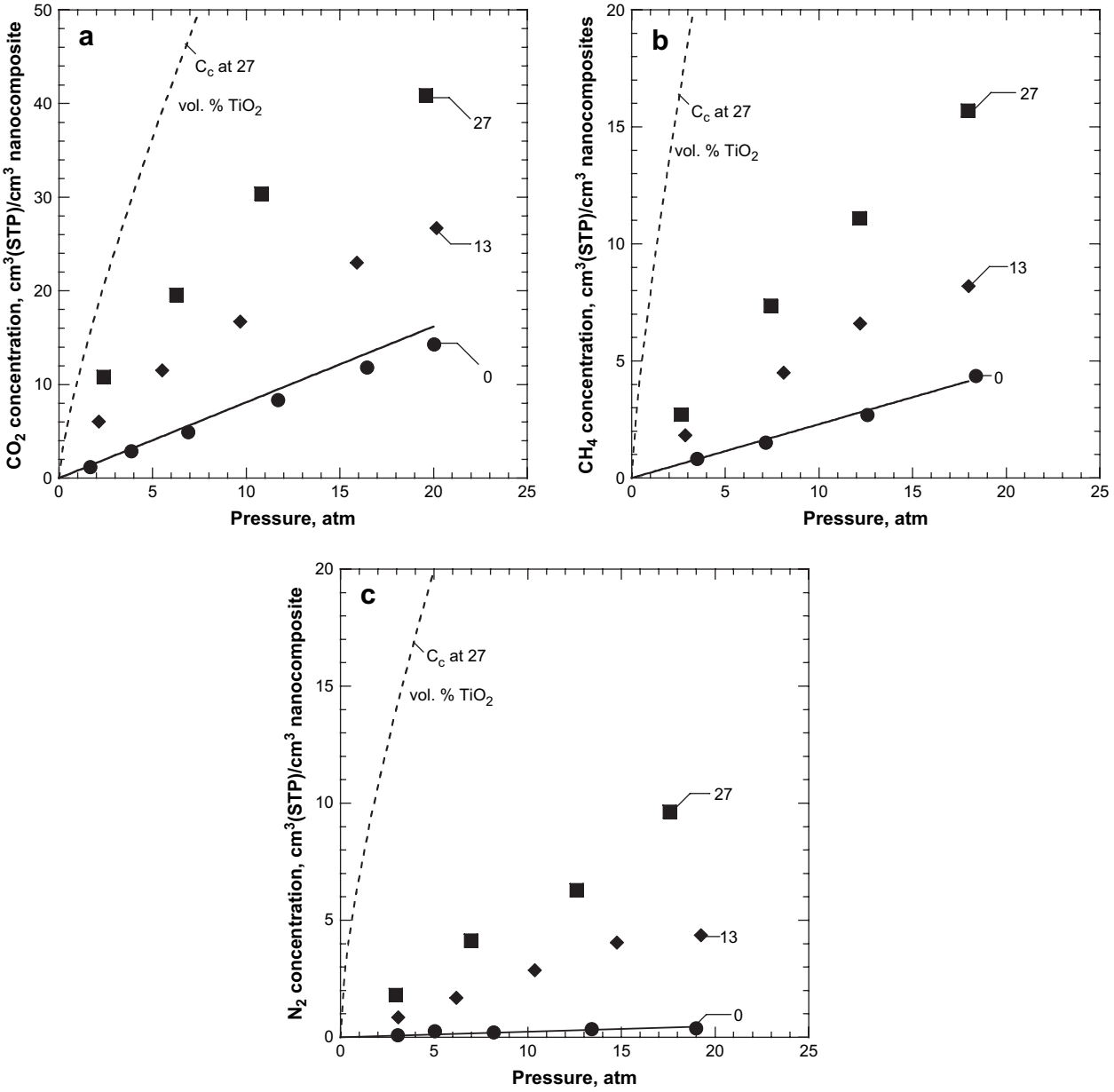

Fig. 14. Sorption isotherms at 35 °C for (a) CO_2, (b) CH_4, and (c) N_2 in PB containing 0 (●), 13 (◆), and 27 (■) nominal volume percent TiO_2. The dashed line represents the estimated gas concentration in the nanocomposite, C_C, according to Eq. (33) for a PB film containing 27 nominal volume percent TiO_2. The solid line represents gas concentration in unfilled PB from the work of Naito et al. [48].

5 vol% voids), the polymer phase contribution to CO_2 and CH_4 concentrations is approximately 24 and 7 times higher than that of the voids, respectively. However, for low sorbing gases such as N_2, the contribution of the voids may be similar to or greater than that of the polymer. For example, in a film containing 20 nominal volume percent TiO_2, the concentration of N_2 in the polymer is roughly equivalent to that in the void space. However, when C_f is extrapolated to pressures greater than atmospheric, the nanoparticles are estimated to adsorb almost two orders of magnitude more gas than either the polymer or the voids, so the particle contribution to the overall concentration of gas sorbed in the nanocomposite, as estimated by Eq. (33), is the dominant contribution to gas uptake in the nanocomposites.

As shown in Fig. 14, the gas concentration in the nanocomposite predicted by Eq. (33) overestimates gas concentration in the nanocomposites. Eq. (33) does not account for the influence of polymer–particle interactions on gas sorption levels. Similar non-additive solubility behavior has been reported for gas solubility in natural rubber filled with micron-sized ZnO [1]. This behavior was attributed to polymer adsorption on the particle surface, which restricts the ability for penetrant gases to sorb on the particle surface [1]. Also, the light gas sorption isotherms in the nanocomposites do not increase linearly with increasing pressure, as expected of gas sorption in polymer alone. The curvature in the influence of gas sorption isotherms presumably derives from the sorption of gases on the nanoparticle surface on the overall gas uptake in the

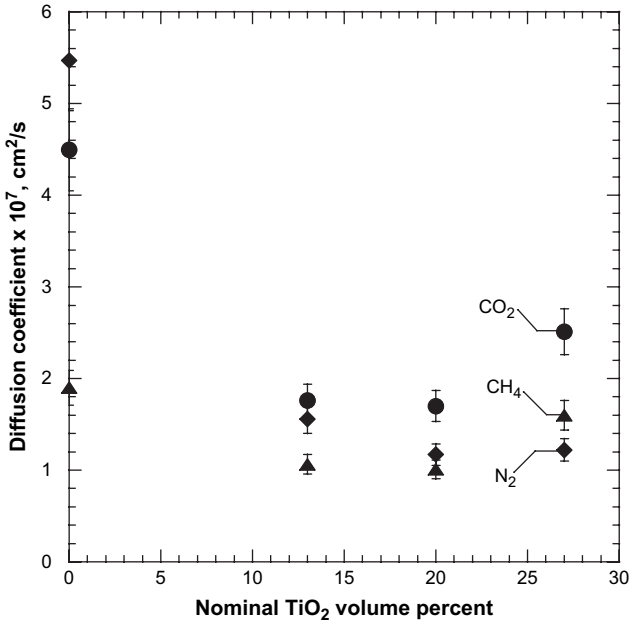

Fig. 15. Concentration-averaged diffusion coefficients for CO_2 (●), CH_4 (▲), and N_2 (◆) as a function of TiO_2 content. Diffusivity was calculated from Eq. (2), using permeability data measure at 35 °C and $\Delta p = 4.4$ atm. Solubility was estimated by linearly interpolating the concentration data to 4.4 atm and using Eq. (3). Error bars were estimated from permeability and solubility according to the propagation of errors method [39].

samples. Additionally, the gas sorption isotherms on the particles are only available up to 1 atm, so the model is being extrapolated to much higher pressure than where experimental data are available for the gas sorption on the particles, so any inaccuracy in that extrapolation would also contribute to the observed differences between the model and the experimental data.

Fig. 14 also shows that the gas concentration in the nanocomposites is higher than that in the polymer. For example, in films containing 27 nominal volume percent TiO_2, the CO_2, CH_4, and N_2 gas concentrations are 2.7, 4, and 18 times higher, respectively, than in the unfilled PB at ~18 atm. The ratio of gas concentration in the nanocomposite to that in the unfilled polymer changes substantially from one gas to another. These differences are ascribed to the difference between the amount of gas that can be adsorbed on the neat particle surface relative to the amount of gas that sorbs in the unfilled polymer. That is, the neat nanoparticles adsorb approximately 70, 170, and 1600 times more CO_2, CH_4, and N_2 than the unfilled PB, respectively, at 1 atm. It is reasonable that the ratio of the gas concentration in the nanocomposites to that in unfilled PB varies from one gas to another.

Using the measured permeability and gas sorption coefficients, gas diffusion coefficients were calculated as a function of particle loading. Nanoparticles have been reported to increase diffusion coefficients, as in brookite filled PTMSP [8], or decrease diffusivity as in PTMSP filled with trimethylsilylglucose [52]. Many studies of transport in heterogeneous systems and the standard composite models of transport in polymer/particle mixtures suggest that impermeable particles in polymers decrease diffusion coefficients by increasing the tortuosity of the pathway that diffusing gas molecules must travel to traverse a polymer film [1,2,44].

Diffusion coefficients were calculated from Eq. (2), using permeability coefficients measured at 35 °C and $\Delta p = 4.4$ atm. Solubility was estimated by linearly interpolating the concentration data to 4.4 atm and using Eq. (3). Fig. 15 presents the results of these calculations. In all cases, gas diffusivity initially decreases substantially with increasing particle loading before increasing slightly at the highest loadings considered. These data suggest a competition between particle-induced increases in tortuosity at lower loadings, which reduce diffusion coefficients, and the increasing contribution of voids at high particle loadings, which increases diffusion coefficients. Additionally, the effect of decreasing crystallinity and increasing T_g in the nanocomposites should influence diffusion coefficients though it was not possible to isolate these factors. The net result of somewhat lower diffusivity and significantly enhanced solubility is a 3–4-fold increase in gas permeability as nanoparticle content increases.

5. Conclusions

TiO_2 nanoparticles were dispersed in 1,2-polybutadiene via solution processing, resulting in particle aggregates ranging in characteristic diameter from nanometers to microns. The nanocomposites exhibit density values below those predicted by an additive density model, suggesting the presence of voids within the nanocomposite films. Gas permeability is 3–4 times higher in 1,2-polybutadiene filled with TiO_2 than in the unfilled polymer. This permeability enhancement is due to an increase in gas solubility coefficients in the nanocomposite films. Diffusion coefficients initially decrease with increasing particle loading, presumably due to the increase in tortuosity caused by the presence of substantial amounts of impermeable particles in the nanocomposites, and then increase at the highest loadings considered.

Acknowledgements

We gratefully acknowledge partial support of this work by the U.S. Department of Energy (Grant No. DE-FG03-02ER15362), the Welch Foundation, and the National Science Foundation (CBET 0515425). The authors would also like to warmly acknowledge Steve Werner and Dr. Jing Li of the Dow Chemical Company for sharing their expertise regarding AFM sample preparation and experimental procedures.

References

[1] Barrer RM, Barrie JA, Rogers MG. Heterogeneous membranes: diffusion in filled rubber. Journal of Polymer Science, Part A: Polymer Chemistry 1963;1:2565–86.
[2] Lape NK, Nuxoll EE, Cussler EL. Polydisperse flakes in barrier films. Journal of Membrane Science 2004;236:29–37.
[3] Wang ZF, Wang B, Qi N, Zhang HF, Zhang LQ. Influence of fillers on free volume and gas barrier properties in styrene–butadiene rubber studied by positrons. Polymer 2005;46:719–24.

[4] Krook M, Morgan G, Hedenqvist MS. Barrier and mechanical properties of injection molded montmorillonite/polyesteramide nanocomposites. Polymer Engineering and Science 2005;45:135–41.
[5] Matteucci S, van Wagner E, Swinnea S, Freeman BD, Sakaguchi T, Masuda T. Desilylation of substituted polyacetylenes in the presence of nanoparticles. Macromolecules 2007;40:3337–47.
[6] Merkel TC, Freeman BD, Spontak RJ, He Z, Pinnau I, Meakin P, et al. Ultrapermeable, reverse-selective nanocomposite membranes. Science 2002;296:519–22.
[7] Merkel TC, He Z, Pinnau I, Freeman BD, Meakin P, Hill AJ. Sorption and transport in poly(2,2-bis(trifluoromethyl)-4,5-difluoro-1,3-dioxole-*co*-tetrafluoroethylene) containing nanoscale fumed silica. Macromolecules 2003;36:8406–14.
[8] Matteucci S, Kusuma V, Sanders D, Swinnea S, Freeman BD. Gas transport in TiO_2 nanoparticle filled poly(1-trimethylsilyl-1-propyne. Journal of Membrane Science 2008;307:196–217.
[9] Matteucci S, Kusuma V, Kelman S, Freeman BD. Gas transport properties in MgO nanoparticle filled poly(1-trimethylsilyl-1-propyne). Polymer, submitted for publication.
[10] Merkel TC, Freeman BD, Spontak RJ, He Z, Pinnau I, Meakin P, et al. Sorption, transport, and structural evidence for enhanced free volume in poly(4-methyl-2-pentyne)/fumed silica nanocomposite membranes. Chemistry of Materials 2003;15:109–23.
[11] Takahashi S, Paul DR. Gas permeation in poly(ether imide) nanocomposite membranes based on surface-treated silica. Part 1: without chemical coupling to matrix. Polymer 2006;47:7519–34.
[12] Patel NP, Miller AC, Spontak RJ. Highly CO_2-permeable and -selective membranes derived from crosslinked poly(ethylene glycol) and its nanocomposites. Advanced Functional Materials 2004;15:699–707.
[13] Matteucci S, Yampol'skii YP, Freeman BD, Pinnau I. Transport of gases and vapors in glassy and rubbery polymers. In: Yampol'skii YP, Freeman BD, Pinnau I, editors. Materials science of membranes for gas and vapor separations. London: John Wiley and Sons; 2006. p. 1–48.
[14] Freeman BD, Pinnau I. Polymeric materials for gas separations. In: Freeman BD, Pinnau I, editors. Polymer membranes for gas and vapor separation. ACS symposium series, vol. 733. Washington, DC; 1999. p. 1–27.
[15] Petropoulos JH. Mechanisms and theories for sorption and diffusion of gases in polymers. In: Paul DR, Yampol'skii YP, editors. Polymeric gas separation membranes. Boca Raton: CRC Press, Inc.; 1994. p. 17–82.
[16] Petropoulos JH. A comparative study of approaches applied to the permeability of binary composite polymeric materials. Journal of Polymer Science Polymer Physics Edition 1985;23:1309–24.
[17] Bouma RHB, Checchetti A, Chidichimo G, Drioli E. Permeation through a heterogeneous membrane: the effect of the dispersed phase. Journal of Membrane Science 1997;128:141–9.
[18] Vu DQ, Koros WJ, Miller SJ. Mixed matrix membranes using carbon molecular sieves II. Modeling permeation behavior. Journal of Membrane Science 2003;211:335–48.
[19] Obata Y, Tosaki C, Ikeyama M. Bulk properties of syndiotactic 1,2-polybutadiene. I. Thermal and viscoelastic properties. Polymer Journal 1975;7:207–16.
[20] Natta G. Determination of the polypropylene crystallinity. Atti della Accademia Nazionale dei Lincei Rendiconti-Classe de Scienze Fisiche-Matematiche e Naturali 1957;22:11–7.
[21] Dhoot SN, Freeman BD, Stewart M, Hill AJ. Sorption and transport of linear alkane hydrocarbons in biaxially oriented poly(ethylene terephthalate). Journal of Polymer Science, Part B: Polymer Physics 2001;39:1160–72.
[22] Lin H, Freeman BD. Gas solubility, diffusivity and permeability in poly(ethylene oxide). Journal of Membrane Science 2004;239:105–17.
[23] Natta G, Corradini P. The structure of crystalline 1,2-polybutadiene and of other "syndiotactic polymers". Journal of Polymer Science 1956;20:251–66.
[24] Olkin I, Gleser LJ, Derman C. Probability models and applications. 2nd ed. New York: Macmillan College Publishing Company; 1980. p. 444–53.
[25] Bondar VI, Freeman BD, Pinnau I. Gas sorption and characterization of poly(ether-*b*-amide) segmented block copolymers. Journal of Polymer Science, Part B: Polymer Physics 1999;37:2463–75.
[26] Wiederhorn S, Fields R, Low S, Bahng G, Wehrstedt A, Hahn J, et al. Mechanical properties. In: Czichos H, Smith LE, Saito T, editors. Springer handbook of materials measurement methods. Springer; 2005. p. 283–397.
[27] Bondar V, Freeman BD, Pinnau I. Gas transport properties of poly(ether-*b*-amide) segmented block copolymers. Journal of Polymer Science, Part B: Polymer Physics 2000;38:2051–62.
[28] Utamapanya S, Klabunde KJ, Schlup JR. Nanoscale metal oxide particles/clusters as chemical reagents. Synthesis and properties of ultrahigh surface area magnesium hydroxide and magnesium oxide. Chemistry of Materials 1991;3:175–81.
[29] Liu L, Qi Z, Zhu X. Studies on nylon 6/clay nanocomposites by melt-intercalation process. Journal of Applied Polymer Science 1998;71:1133–8.
[30] Chaudhary DS, Prasad R, Gupta RK, Bhatacharya SN. Clay intercalation and influence on crystallinity of EVA-based clay nanocomposites. Thermochimica Acta 2005;433:187–95.
[31] Tasagaropoulos G, Eisenberg A. Dynamic mechanical study of the factors affecting the two glass transition behavior of filled polymers. Similarities and differences with random ionomers. Macromolecules 1995;28:6067–77.
[32] Rittigstein P, Torkelson JM. Polymer–nanocomposite interfacial interactions in polymer nanocomposites: confinement effects on glass transition temperature and suppression of physical aging. Journal of Polymer Science, Part B: Polymer Physics 2006;44:2935–43.
[33] Takahashi S, Goldberg HA, Feeney CA, Karim DP, Farrell M, O'Leary K, et al. Gas barrier properties of butyl rubber/vermiculite nanocomposite coatings. Polymer 2006;47:3083–93.
[34] Wan T, Wang Y-C, Feng F. Preparation of titanium dioxide/polyacrylate nanocomposites by sol–gel process in reverse micelles and *in situ* photopolymerization. Journal of Applied Polymer Science 2006;102:5105–12.
[35] Stark RW, Drobek T, Heckl WM. Tapping-mode atomic force microscopy and phase-imaging in higher eigenmodes. Applied Physics Letters 1999;74:3296–8.
[36] Sengupta R, Bandyopadhyay A, Sabharwal S, Chaki TK, Bhomick AK. Polyamide-6,6/in situ silica hybrid nanocomposites by sol–gel technique: synthesis, characterization, and properties. Polymer 2005;46:3343–54.
[37] Ma D, Akpalu YA, Li Y, Siegel RW, Schadler LS. Effect of titania nanoparticles on the morphology of low density polyethylene. Journal of Polymer Science, Part B: Polymer Physics 2005;43:488–97.
[38] Yang H, Bhimaraj P, Yang L, Siegel RW, Schadler LS. Crystal growth in alumina/poly(ethylene terephthalate) nanocomposite films. Journal of Polymer Science, Part B: Polymer Physics 2007;45:747–57.
[39] Bevington PR, Robinson DK. Data reduction and error analysis for the physical sciences. 3rd ed. New York: McGraw-Hill, Inc.; 2003.
[40] Weibull W. A statistical distribution function of wide applicability. Journal of Applied Mechanics 1951;18:293–7.
[41] Mackay ME, Dao TT, Tuteja A, Ho DL, Van Horn B, Kim H-C, et al. Nanoscale effects leading to non-Einstein-like decrease in viscosity. Nature Materials 2003;2:762–6.
[42] Gestoso P, Nicol E, Doxastakis M, Theodorou DN. Atomistic Monte Carlo simulation of polybutadiene isomers: *cis*-1,4-polybutadiene and 1,2-polybutadiene. Macromolecules 2003;36:6925–38.
[43] Hill RJ. Diffusive permeability and selectivity of nanocomposite membranes. Industrial and Engineering Chemistry Research 2006;45:6890–8.
[44] Barrer RM. Diffusion and permeation in heterogeneous media. In: Crank J, Park GS, editors. Diffusion in polymers. New York: Academic Press; 1968. p. 165–219.
[45] Merkel TC, He Z, Pinnau I, Freeman BD, Hill AJ, Meakin P. Effect of nanoparticles on gas sorption and transport in poly(1-trimethylsilyl-1-propyne). Macromolecules 2003;36:6844–55.
[46] Lindbrathen A, Hagg M-B. Glass membranes for purification of aggressive gases. Part II. Adsorption measurements and diffusion coefficient estimations. Journal of Membrane Science 2005;259:154–60.
[47] Bird RB, Stewart WE, Lightfoot EL. Transport phenomena. 2nd ed. New York: John Wiley & Sons; 2002.

[48] Naito Y, Kamiya Y, Terada K, Mizoguchi K, Wang J-S. Pressure dependence of gas permeability in a rubbery polymer. Journal of Applied Polymer Science 1996;61:945–50.
[49] Do DD. Adsorption analysis: equilibria and kinetics. In: Series on chemical engineering, vol. 2. London: Imperial College Press; 1998.
[50] Weinkauf DH, Paul DR. Effects of structural order on barrier properties. In: Koros WJ, editor. Barrier polymers and structures. ACS symposium series, vol. 423. Washington, DC: American Chemical Society; 1990. p. 60–91.
[51] Michaels AS, Bixler HJ. Solubility of gases in polyethylene. Journal of Polymer Science 1961;50:393–412.
[52] Qiu J, Zheng J-M, Peinemann K-V. Gas transport properties in a novel poly(trimethylsilylpropyne) composite membrane with nanosized organic filler trimethylsilylglucose. Macromolecules 2006;39:4093–100.